

Phase space density distributions of energetic electrons in the outer radiation belt during two Geospace Environment Modeling Inner Magnetosphere/Storms selected storms

Y. Chen,¹ R. H. W. Friedel,¹ and G. D. Reeves¹

Received 3 March 2006; revised 14 July 2006; accepted 12 September 2006; published 30 November 2006.

[1] The phase space density distributions of energetic electrons during two storm periods, including the two storms on 21–23 October 2001 and 4–9 September 2002 selected by Geospace Environment Modeling Inner Magnetosphere/Storms campaign as the radiation belt assessment challenge in 2004 workshop, are presented in this paper. Electron data from the Synchronous Orbit Particle Analysis instrument aboard three Los Alamos National Laboratory geosynchronous satellites as well as the Comprehensive Energetic Particle and Pitch Angle Distribution instrument aboard Polar are used. The Tsyganenko 2001 storm model is chosen for the storm time magnetic field presentation, compared to the best-fitting magnetic model achieved in a previous study. By tracing the temporally evolving radial distributions, we conclude that while the dropout of electron phase space density during storm main phases appears to be energy-independent, the enhancement in recovery phases shows an energy-dependent pattern. The average outwardly decreasing radial gradients of phase space density obtained during the recovery phases of the two storm periods strongly suggest the in situ acceleration is most likely the main source of new energetic electrons, along with a possible contribution from an external source.

Citation: Chen, Y., R. H. W. Friedel, and G. D. Reeves (2006), Phase space density distributions of energetic electrons in the outer radiation belt during two Geospace Environment Modeling Inner Magnetosphere/Storms selected storms, *J. Geophys. Res.*, *111*, A11S04, doi:10.1029/2006JA011703.

1. Introduction

[2] Though it has been widely known that the energetic electron fluxes in the outer radiation belt frequently change significantly during geomagnetic storms (e.g., the review by *Li and Temerin* [2001] and references therein), an unsolved problem is still what physics processes should account for this change. Two possible electron sources have been recognized as being able to refill the depleted radiation belts after a storm main phase: One source is the electrons initially in the tail portion being transported inwardly and energized by betatron acceleration, also known as an external source; the other is the less energetic electrons being accelerated by in situ acceleration inside the inner magnetosphere, i.e., an internal source. Theories and models have been developed along these two directions, and details can be found in the review paper by *Friedel et al.* [2002]. To differentiate these two sources is not an easy task, due to the lack of enough data with well-coordinated and long-term coverage as well as the difficulty that the loss and energization physical processes occur simultaneously during storm times, and consequently

requires a careful comparison between data and model output.

[3] To coordinate the community's efforts, the Inner Magnetosphere/Storms (IM/S) campaign of the Geospace Environment Modeling (GEM) program decided to choose two storm periods, 21–23 October 2001 and 4–9 September 2002, on which data analyzers and modelers can work together. This paper aims to provide a brief description of the electron phase space density (PSD) distributions during the two storms, while the complete data sets are available via ftp from the Web site ftp://ftp.nsstc.org/gem/rad_belt_challenge.

[4] The study of the PSD at constant adiabatic invariants has the advantage over the traditional study of fluxes in a spatial coordinate frame in that the former separates nonadiabatic effects from adiabatic ones (e.g., the Dst effect [*Kim and Chan*, 1997]), and is the appropriate way to relate measurements from different regions in the inner magnetosphere. Since the radial diffusion equation determines that electrons can only diffuse from drift shells with large PSD toward those with small PSD [*Schulz and Lanzerotti*, 1974], tracing the temporally evolving electron phase space density radial profile can help to reveal the locations of the source (the maximum point(s) in a PSD radial profile) and the sink (the minimum point(s)). As shown in Figure 2 of *Green and Kivelson* [2004], the case of an external source requires a

¹Los Alamos National Laboratory, Los Alamos, New Mexico, USA.

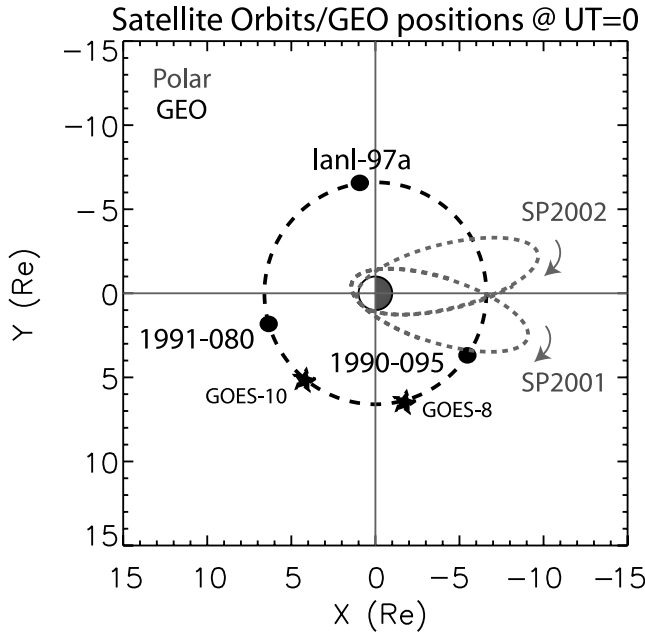


Figure 1. Orbits of LANL GEO (black) and Polar (gray) in the GSE xy plane during the storm period in 2001 (SP2001) and 2002 (SP2002). The Polar orbit plane moves clockwise (the direction of the gray arrows) during the course of each year. The local time positions of LANL GEO at UT = 0000 are plotted, along with two GOES satellites.

positive PSD radial gradient, i.e., PSD increasing radially outward, while in situ energized electrons produce a local peak and negative gradients, allowing them to diffuse outward.

[5] A brief description of the instrumentation and data is presented in section 2. Section 3 presents the method, the intercalibration, the magnetic field models, and the PSD distribution results. A discussion of the results follows in section 4 and conclusions in section 5.

2. Instrumentation and Data

[6] The electron flux $j(E, \alpha, \vec{r}, t)$ is a function of energy E , local pitch angle α , satellite position \vec{r} and time t , while the PSD $f(\mu, K, L^*, t)$ is the temporally varying distribution density in a phase space labeled by the three phase space momentum coordinates: The first adiabatic invariant μ , the second adiabatic invariant K and the drift shell L^* associated with the third adiabatic invariant. Flux is converted into PSD from $f = j/p^2$, where p is the magnitude of the relativistic momentum corresponding to the kinetic energy E and also the perpendicular component of p to the local magnetic field is associated with μ [Schulz and Lanzerotti, 1974]. Therefore to obtain the distribution of PSD at given adiabatic invariants, we first need the angular resolved electron fluxes and local magnetic field magnitude for each of the satellites. In addition, to calculate the values of K and L^* , we also need the global configuration of the magnetic field that can be provided by models only. Readers are referred to Appendix A and Chen et al. [2005] for details on the calculation of PSD and adiabatic invariants.

[7] In this work, aboard each of the three Los Alamos National Laboratory geosynchronous (LANL GEO) satellites (1990-095, 1991-080, and LANL-97A), the Synchronous Orbit Particle Analysis (SOPA) instrument [Belian et al., 1992; Reeves et al., 1997] can measure the full three-dimensional electron distribution from 50 keV to more than 1.5 MeV in each spin. Since the LANL GEO satellites carry no magnetometer instruments, we employ the method developed by Thomsen et al. [1996] through which the local magnetic field direction can be derived from the measurement of the plasma distribution by another instrument on board, the Magnetospheric Plasma Analyzer (MPA), to obtain the pitch angle distribution. A detailed description of the derivation of the pitch angle distribution can be found in the Chen et al. [2005]. In this work the LANL GEO electron data have a 10-minute time resolution. For the local magnetic field magnitude we use values from an empirical magnetic field model.

[8] With a polar orbit of $2 \times 9 R_E$, Polar crosses the magnetic equatorial plane every ~ 18 hours outside GEO orbit. The Comprehensive Energetic Particle and Pitch Angle Distribution (CEPPAD) experiment [Blake et al., 1995] on board Polar provides angular resolved flux data of energetic electrons, covering the energy range from 30 keV to 10 MeV with the nine detectors of the IES and the one detector of the HIST subsystems. Flux data here have a time resolution of 3.2 min. Polar also carries a Magnetic Field Experiment (MFE) [Russell et al., 1995] measuring magnetic field vectors, which provide the convenience of calculating the first adiabatic invariant.

[9] Figure 1 presents Polar's orbit in one period during each of the two GEM IM/S selected storms, projected into the x-y plane of the GSE coordinate system. Electron data used in this work are mainly from the orbit portion close to apogee. When the Earth revolves around the Sun, Polar has its orbit plane moving $\sim 1^\circ$ clockwise each day during the course of each year and crosses the equatorial plane around midnight in September and October. The local time positions for LANL GEO satellites at UT = 0 hours are also plotted in the same figure, along with those of two GOES satellites.

3. PSD Distributions During Quiet Times and Two Storm Periods

3.1. Methodology, Intersatellite Calibration, and Magnetic Field Model

[10] We follow the method developed previously [Chen et al., 2005] to transform fluxes from multiple satellites to phase space density distributions. This method includes two steps to reduce errors: The first is a test of intersatellite calibration during the quiet time and then the second is the choice of the magnetic field model during storm periods.

[11] Before calculating gradients we first verify the instrument calibration between satellites. The intercalibration between the three LANL GEO satellites has been obtained by Chen et al. [2005] by doing the PSD matching, that is, comparing the PSD values of electrons with the same combination of (μ, K, L^*) but measured by satellites at different spatial locations during magnetically quiet times. Following the same procedure, we obtain the inter calibration between LANL GEO and Polar, and the results are presented in Figure 2. The selected quiet days are 10–13 December

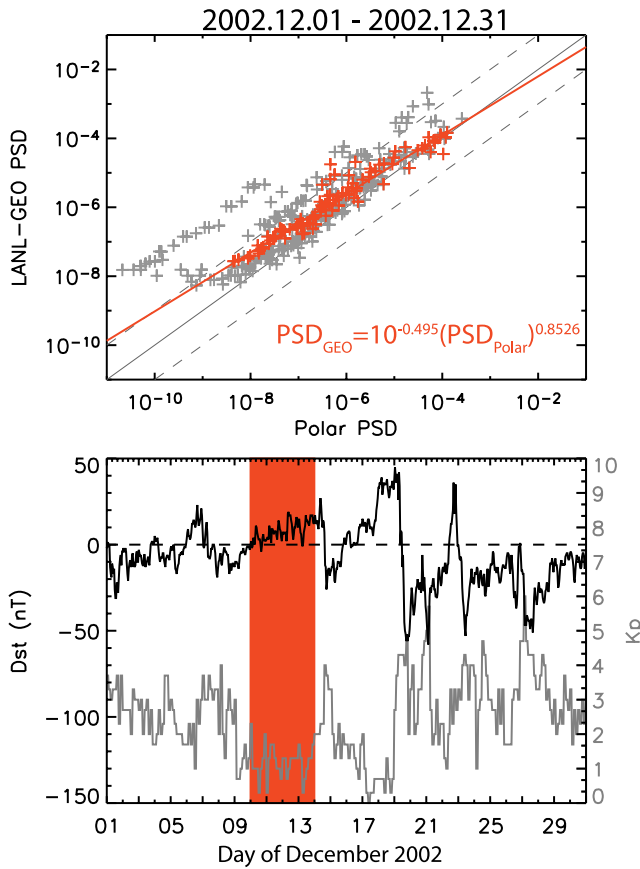


Figure 2. PSD matching between Polar and 1990-095 (top) as well as the Dst and Kp time series during December 2002 (bottom). The unit of PSD is $(c/MeV/cm)^3$. In the upper panel, the red symbols are obtained on quiet days (the period being boxed in red in the lower panel) and gray symbols are for the whole month. The red straight line fits the red symbols and the equation is given in the lower right corner. The diagonal in gray represents perfect intercalibration and the two dashed lines on both sides are for PSD values 10 times larger/smaller.

2002, the area boxed in red in the lower panel of Figure 2, when Polar had its apogee around the duskside of the magnetosphere. Red symbols in the upper panel compare the PSD values from Polar and 1990-095, whose orbits were in such positions that both could sample electrons sharing the same drift shell. All red symbols are already quite close to the gray solid diagonal showing perfect calibration. This is expected since the preliminary intercalibration between Polar and LANL GEO fluxes has already been done [Friedel *et al.*, 2005] and is applied here before the fluxes are transformed into PSD. Fitting by the red straight line, we achieve the intercalibration between Polar and GEO PSD values, the equation in the upper panel, that will be used for storm times. This comparison covers a wide energy range at geosynchronous orbit, from 100 keV up to 1.5 MeV. For reference, PSD values during the whole month of December 2002, during which quite a few storms occurred, are also plotted as gray symbols. Those gray symbols scatter almost symmetrically, though in a broader range, on both sides of the red fitting curve due to various reasons, including the local loss,

acceleration, and erroneous magnetic field description in storm times. Such a symmetric distribution indicates that we have a reasonably good intercalibration.

[12] As for the global magnetic field model, we mainly use the Tsyganenko 2001 storm model (T01s) [Tsyganenko, 2002a, 2002b; Tsyganenko *et al.*, 2003], which stands out from a list of models from a statistical study recently completed (Appendix B). We also tested the best-fitting model, which is obtained by choosing the best performer from a list of existing models by fitting to multipoint local magnetic field measurements during each short time bin. Details about this model are described in Appendix B. The major shortcoming of using the best-fitting model is the discontinuity in the time series of L^* , which arises due to the lack of L^* normalization between existing magnetic field models. Therefore we focus on the results based on T01s model in this paper.

3.2. PSD Distribution During Quiet Time

[13] After the intercalibrations have been applied, the PSD radial distributions during those quiet days in Figure 2 are presented by Figure 3. Three μ values, 167, 1051, and 2083 MeV/G, which approximately correspond to electron energies of ≥ 120 , ≥ 600 , and ≥ 1000 keV at GEO orbit, respectively, are used to represent low-, moderate-, and high-energy cases. The second adiabatic K is chosen to have a value that is small enough to ensure the measured electrons being bounced close to the magnetic equator, where the magnetic field model performs relatively well, and is not too small for Polar to provide enough data points covering a broad range of L^* as well. The K here has a value of $0.1 G^{1/2} R_E$, which corresponds to $\sim 45^\circ$ of equatorial pitch angle for LANL GEO and $\sim 30^\circ$ for Polar.

[14] In Figure 3 we see the diurnal variation of L^* for GEO caused by the asymmetric magnetic field, with larger L^* measured on the nightside where the field is more stretched and weaker than on the dayside. The amplitude of this variation can be as large as ~ 0.5 for 1990-095, which stays furthest away from the magnetic equator among the three LANL GEO satellites. This variation dominates the change of L^* during quiet time and has already been discussed by Chen *et al.* [2005]. That no obvious change in the magnetic field was observed by GOES-8 and GOES-10 (not shown here) demonstrates the magnetic configuration being stable at GEO orbit on those days. However, this is not the case for Polar, and more variation occurred outside GEO orbit. During the same time period, around the apogee portion of its orbit, Polar crossed the outer radiation belt several times, with L^* ranging from ~ 6.5 up to 10 and varying significantly even during this so-called quiet time. This variation comes along with changes of magnetic field observed by Polar. For example, magnetic field observed by Polar (not shown here) is more stretched at crossings 1, 2, 5, and 6 (with larger magnetic field polar angles $\sim 25^\circ$) than at crossings 3, 4, and 7 (with smaller polar angles $\sim 5^\circ$), though Dst and Kp show no significant change.

[15] There was a minor storm occurring before this quiet time period (see the lower panel in Figure 2) with the main phase ending on day 8 of December, and PSD experienced a fast enhancement in the early recovery phase (not shown here). Starting from day 9, already the late recovery phase of the storm as shown in Figure 3, GEO electron PSD with low energy (Figure 3a) decays slowly, while PSD values for

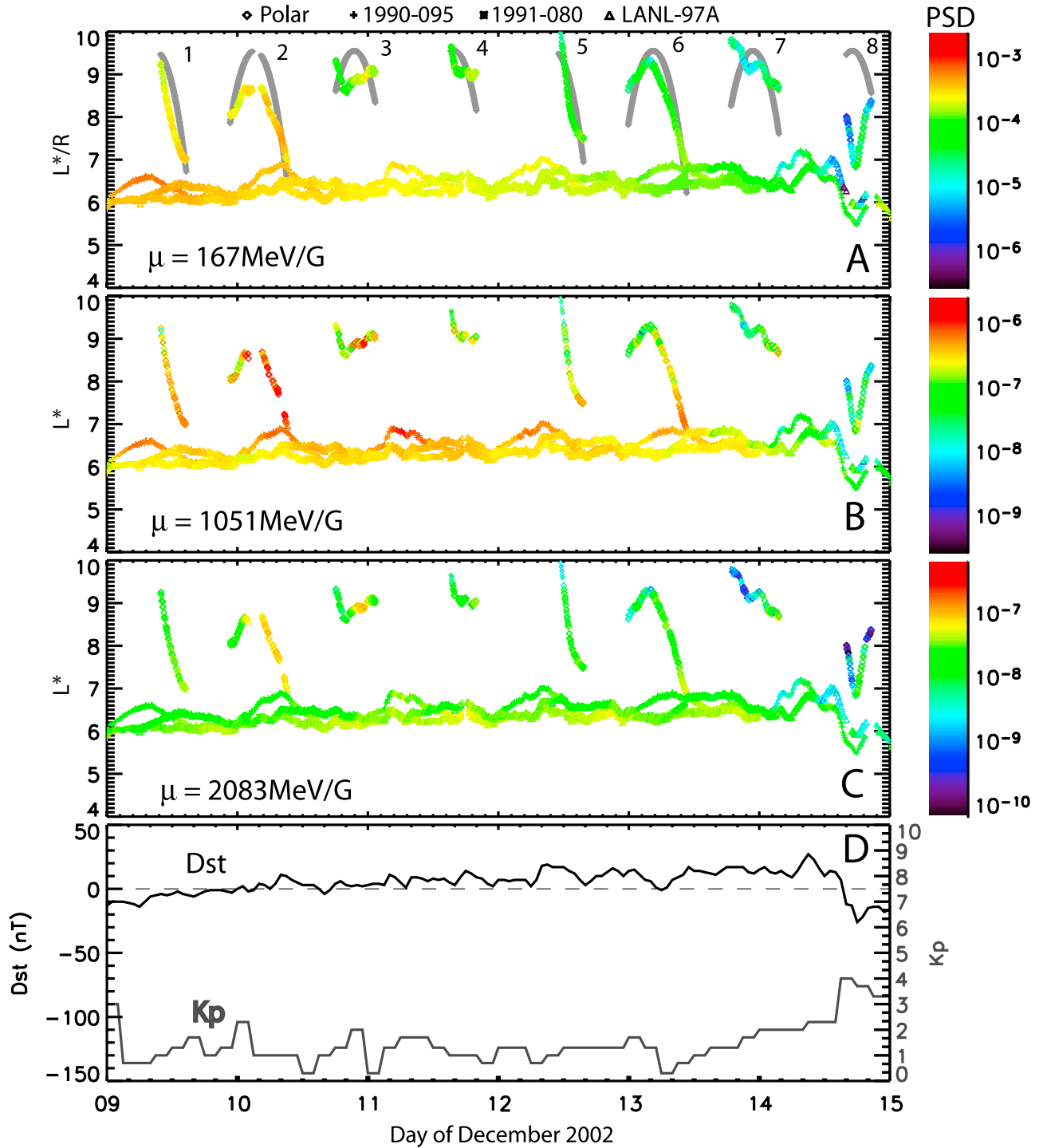


Figure 3. PSD radial distributions during quiet time. From top to bottom, (a, b, c) the PSD versus L^* changing with time for $\mu = 167$, 1051, and 2083 MeV/G, respectively, and (d) the Dst (black) and Kp (gray) curves. The value of the second adiabatic invariant K is $0.1 G^{1/2} R_E$. The PSD value is color-coded with the unit of $(\text{c}/\text{MeV}/\text{cm})^3$. In Figure 3a the radial distances of Polar (the numbered gray curves) from the Earth are given when the PSD and L^* values with the specified (μ, K) are available.

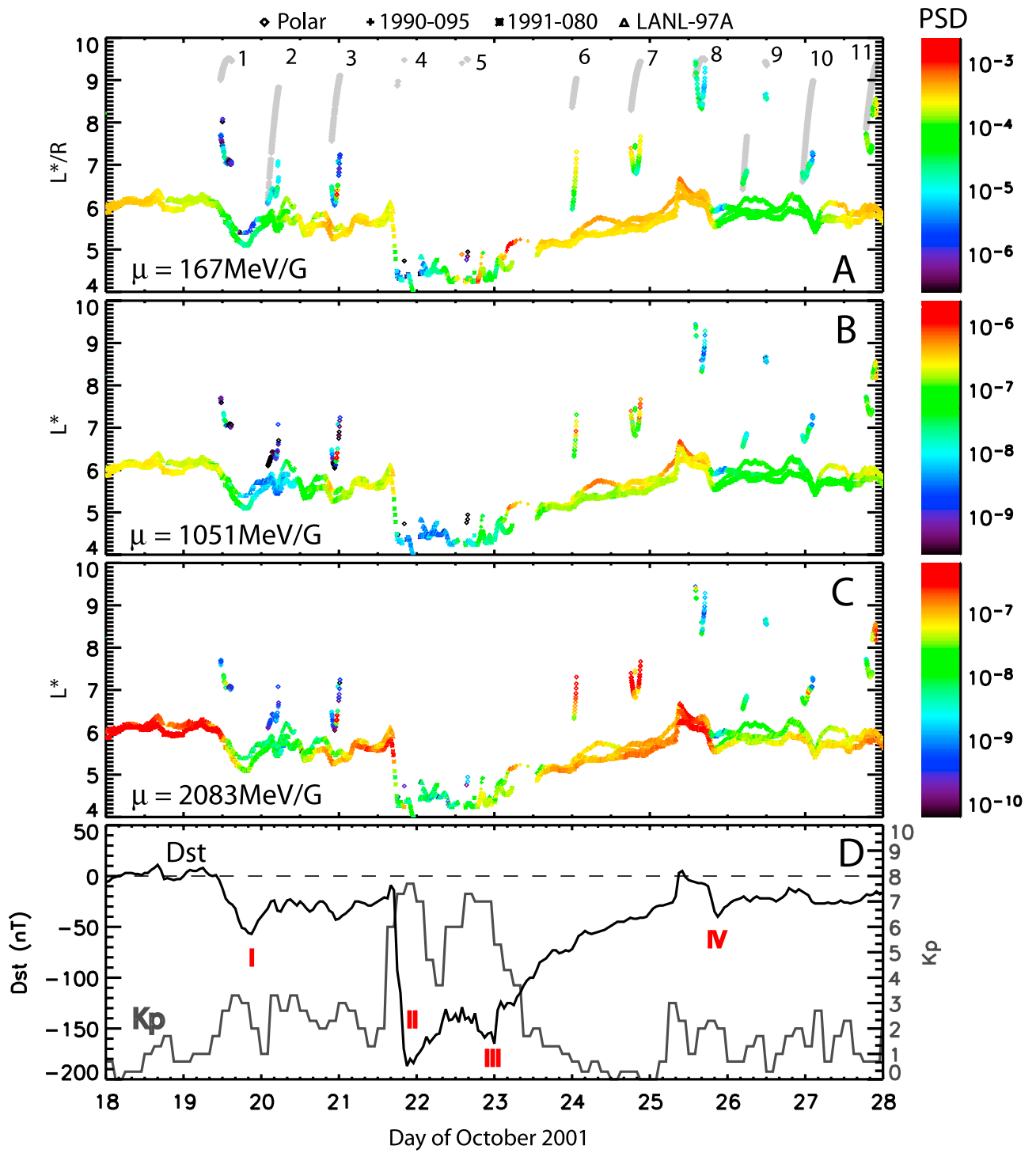


Figure 4. PSD radial distributions during the storm period of year 2001 (SP2001). The same format, μ 's and K values as in Figure 3 are used. Four storms are numbered in red in Figure 4d.

electrons with higher energy (Figures 3b and 3c) seem to be in a stable state. This energy-dependent feature is also seen in the radial gradient: The higher the energy, the more negative the gradient. As for Polar, more variations are seen in the rim of the outer radiation belt: Its PSD increases first at crossings 1 and 2 and then slowly decreases, especially for shells with large L^* .

[16] Focusing on the two quietest days of 11 and 12 in December 2001, we see that in Figure 3 the radial gradients for electrons with the lowest and moderate energies (Panels A and B) strongly suggest a maximum point somewhere between GEO and Polar, whereas the flat or even negative gradients for electrons with high energy suggest a maximum point on or inside GEO orbit, as is consistent with our previous conclusions based exclusively on GEO data [Chen *et al.*, 2005]. Results in Figure 3 are to be compared with distributions during storms presented in the following subsections.

3.3. Storm Period of Year 2001

[17] Including the first GEM IM/S selected storms on 21–23 October 2001, the storm period shown in Figure 4 covers 10 days, ranging from 18 October to 28 October. This period is referred as SP2001 hereinafter. During this period, Polar sampled the nightside radiation belt at local time ~ 22 hours (Figure 1). The curves of PSD versus L^* and time for three μ values are presented in Figure 4, along with Dst and Kp indexes. Besides the GEM IM/S storms (storms II and III in Figure 4d), two other moderate storms on days 19–20 and days 25–26 can also be identified.

[18] One distinguished feature in Figure 4 is that the L^* positions of satellites vary greatly with time, compared to quiet time. For LANL GEO satellites, after the diurnal change is removed, the residual variation of L^* should be caused by changing magnetospheric current systems (especially the ring current), which simultaneously cause the change in Dst and therefore lead to the “Dst effect” in which electrons move to another spatial position so as to conserve the third adiabatic invariant. For example, the intensification of the ring current in the main phase decreases Dst and increases the absolute value of magnetic field flux $|\phi|$ enclosed by a drift shell originally located on GEO orbit. To conserve the flux, the “Dst effect” requires that drift shell to move radially outward and consequently leaves the GEO satellite to find itself on a new drift shell with smaller L^* value. The same reason makes the GEO satellites move back to the prestorm L^* shells in the recovery phase. Such an explanation is supported by the resemblance between the GEO L^* curve and the Dst curve in Figure 4. As for Polar, its L^* changes with Dst roughly in the same way, with a larger variation in values at crossings. For example, compared to the average L^* value of ~ 8.5 on quiet days, the outward moving drift shells during the main phases made Polar detect electrons with L^* of as low as ~ 4.5 at crossing 4. Such large changes in L^* again justify the importance of comparing PSD in a correct magnetic coordinate system.

[19] Other features of how PSD values evolve during storms can be observed from Figure 4, and we describe the four storms (numbered in red color in Figure 4d) in sequence below. It should be noted that here we identify storms in a loose way. For example, storm II and III in Figure 4 may be treated as one storm in other occasions; however, for the

purpose of making a clear description of changing PSD during the course, here we treat them as two separate storms.

[20] Storm I started at UT ~ 10 hours on day 19, and the minimum Dst (-57 nT) was reached before midnight of the same day; then Dst recovered in an irregular way, probably caused by additional geomagnetic activity (as suggested by Kp), until the main phase of storm II arrived. In storm I, GEO satellites witnessed the dropout of PSD values during the main phase for electrons with all energies, and no recovery of PSD was seen until well into the recovery phase. The comparison between PSD values at the same L^* positions prior to and after minimum Dst shows a nonadiabatic loss. Crossing 2 of Polar in the beginning of day 20 also provides the proof of a real (nonadiabatic) loss of electrons when the Polar PSD value at $L^* \sim 6.2$ is compared to the prestorm one observed by GEO. The recovery for electrons with low μ (Figure 4a) at GEO started ~ 12 hours after the minimum Dst and took about 15 hours to reach the prestorm level (those values on day 18), while the recovery of electrons with higher energies (Figures 4b and 4c) had a later start and was at a slower pace. During Polar’s several crossings, the PSD values at GEO are larger than those at Polar.

[21] In the afternoon of day 21 came storm II, a major storm with a minimum Dst of -186 nT. During about 5 hours of the main phase, GEO moved from $L^* \sim 6$ to ~ 4 , with PSD values decreasing by more than one order of magnitude. At the same time, Polar was also seen to move to positions with much lower L^* . Then PSD started to recover a bit in the short recovery phase until being interrupted by the next storm. Partial recovery in PSD for electrons with low μ (Figure 4a) at GEO was seen after noon of day 22, and Polar at crossing 5 also had a strong recovery followed by an immediate loss.

[22] The main phase of storm III started at noon of day 22 and ended at UT ~ 0 hr on day 23, with a minimum Dst of -165 nT. In the middle of this main phase, at UT ~ 20 hours on day 22, electrons with low μ (Figure 4a) had a fast enhancement observed by both 1990-095 at local time (LT) ~ 18.5 hours and 1991-080 at LT ~ 8 hours and then a loss. LANL-97A had no data on that day. Weaker enhancements were observed for electrons with higher energies. The recovery phase of storm III lasted for more than 2 days. Starting from UT ~ 4 hours on day 23, another fast enhancement in electrons at all energies was observed by 1990-095 with larger L^* at midnight, while 1991-080 with smaller L^* saw no change at local time ~ 17 hours. This can be interpreted as either a positive radial gradient or an injection from the nightside. It is interesting to point out that on the next 2 days of the recovery phase, such a positive gradient was kept for low- and moderate-energy electrons (Figures 4a and 4b) but reversed for high-energy electrons (Figure 4c), with no local time feature. More interestingly, on day 24, at crossings 6 and 7, Polar data by themselves showed positive PSD radial gradients. Combined with the gradients from GEO, it is implied that at least two peaks in the PSD profile exist: One inside the radiation belt (between GEO and Polar for low-energy electrons and inside GEO for high-energy), and the other outside of the Polar orbit. The fact that such a radial distribution for low-energy electrons at GEO lasts for more than one day rules out the possibility of the positive

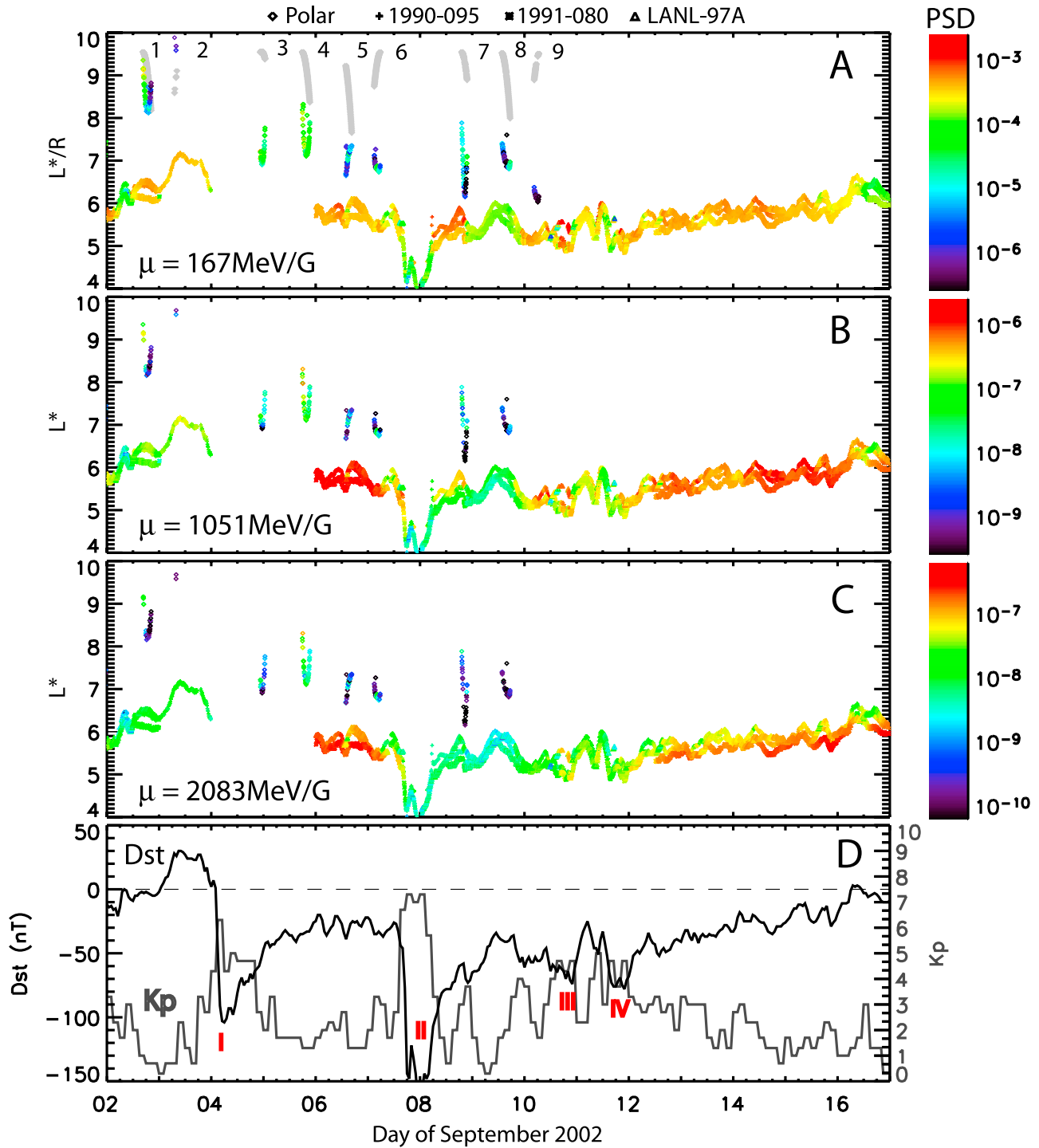


Figure 5. PSD radial distributions during the storm period of year 2002 (SP2002). The same format, μ s, and K values as in Figure 3 are used. In Figure 5d four storms are numbered in red.

gradient being caused by an improper inter calibration between the GEO satellites.

[23] The last storm, storm IV, is a moderate one starting on day 25. Dst stopped decreasing before the end of the day. The loss of PSD at GEO is fast, nonadiabatically dropping by about one order of magnitude in around one hour. The loss was also seen by Polar at the beginning of crossing 9, when Polar had $L^* \sim 6.5$. A strong recovery of

PSD at GEO did not start until day 27 and the same radial gradients as in storm III reappeared. At the end of crossing 11, Polar also detected an increase in PSD, much later than GEO.

3.4. Storm Period of Year 2002

[24] For the storm period of year 2002 (SP2002), the evolving PSD radial distributions are presented in Figure 5,

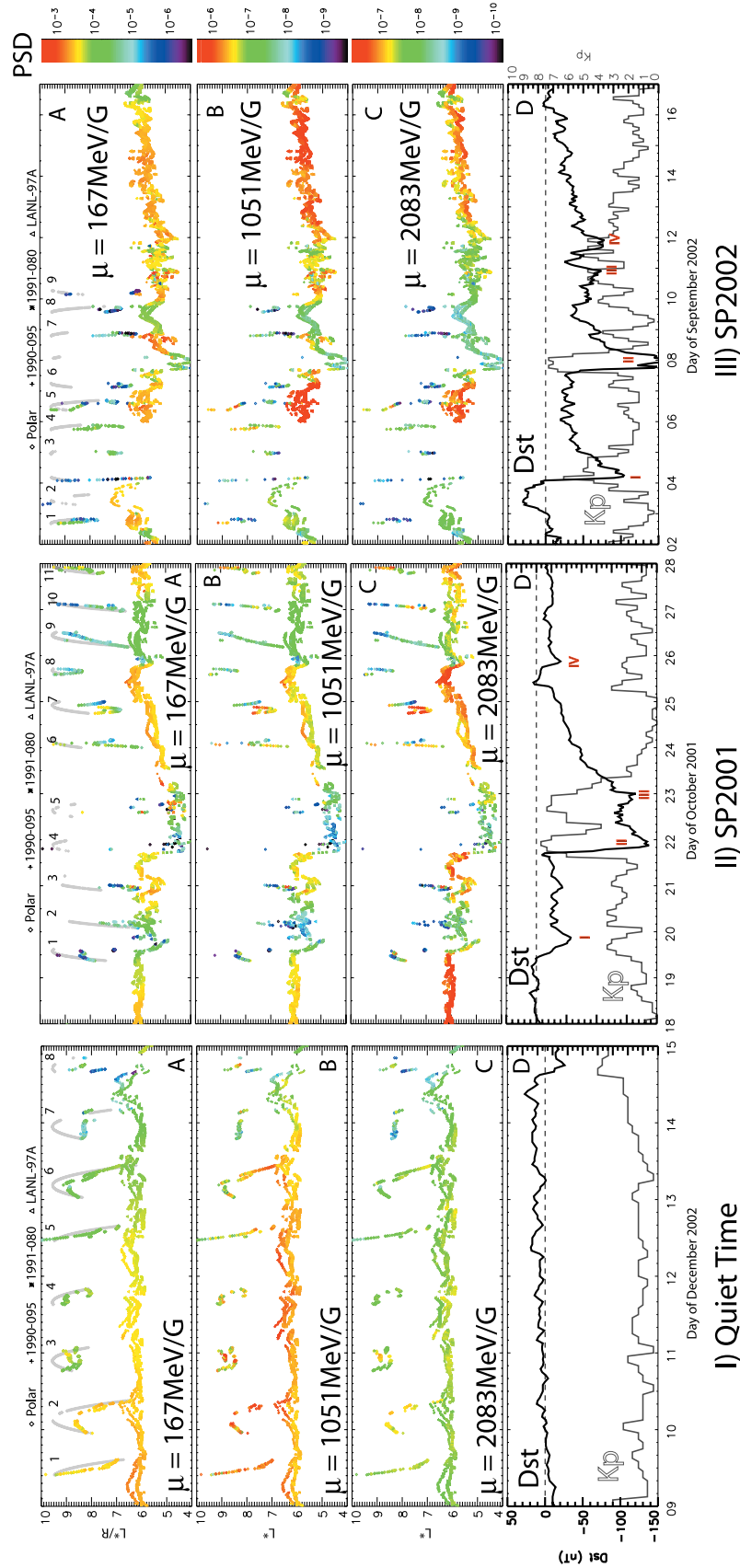


Figure 6. PSD radial distributions during quiet time (column I), SP2001 (column II), and SP2002 (column III). The best-fitting magnetic model (Appendix B) is used here.

which covers 15 days (2–16 September) and includes the second GEM IM/S selected storms on 4–9 September (storms I and II in Figure 5d). In the long recovery phase of storm II, the Dst curve shows complicated structures of which at least two more storms can be identified and are numbered as III and IV. Data coverage in SP2002 is not as good as in SP2001: There are no LANL GEO data during the main phase and early recovery phase of storm I and no Polar data from day 10 until the end of the period. Next we discuss those storms in detail.

[25] Storm I had an initial phase throughout day 3. On that day, GEO moved to positions with larger L^* while PSD values hardly changed, whereas Polar first experienced a significant drop in PSD for electrons with all energies at the end of crossing 1 and then moved to $L^* \sim 9.5$ at crossing 2 when Dst reached ~ 30 nT. At those two crossings Polar had small PSD values compared to those during quiet time, as shown in Figure 3. This may be explained by the loss mechanism called “magnetopause shadowing” [Kanekal *et al.*, 2000] through which drifting electrons are lost when encountering the magnetopause. Next, on day 4 and 5 during the main phase and early recovery phase, the data from Polar at crossings 3 and 4 showed some recovery in PSD. In the rest of the recovery phase, PSD values at GEO were fully recovered and even reached higher levels than prestorm ones for electrons with moderate and high energies (Figures 5b and 5c), while PSD values by Polar again decreased and were always smaller than those at GEO.

[26] The main phase of storm II had two dips in Dst: the first one with a minimum of -148 nT at UT ~ 20 hours on day 7 followed by the second one -167 nT (off scale in Figure 5d) 2 hours later. The PSD values of all electrons at GEO dropped significantly with the first decrease of Dst and stayed constant through the end of the main phase. PSD recovery began hours later than the recovery of Dst and was energy dependent. At the end of day 8, electrons with low-energy finally reached values larger than prestorm ones and had positive radial gradients (Figure 5a), while no obvious recovery was seen for the high-energy electrons (Figure 5c). This energy-dependent recovery was also witnessed by Polar at the first half of crossing 7: Larger increases in PSD of low μ electrons than high μ , compared to values at crossing 6. After this, at UT ~ 23 hours of day 8, a small decrease of Dst started another round of loss in PSD, observed by both GEO and Polar in the second half of crossing 7. This time the recovery of electrons at GEO did not start until about 20 hours later, again with more intensive recovery in the lower energy electrons, while the PSD measured by Polar did not come back at all at crossings 8 and 9. The average PSD at GEO is larger than Polar, i.e., an outward negative radial gradient.

[27] The electron PSD recovery at GEO was disturbed again by storm III and IV. After Dst reached the lowest value at UT ~ 22 hr on day 11, the energy dependent recovery behavior resumed: A fast recovery for electrons with low energy (Figure 5a) and a slow recovery with negative gradients for high energy (Figure 5c). Such radial distributions stayed stable for the rest of the recovery phase. The prominent negative gradients for high-energy electrons make

it a storm that has strong recovery in energetic electrons with a likely internal source.

4. Discussion

4.1. Effects of Magnetic Field Models

[28] An accurate study of electron PSD distribution demands a good knowledge of the magnetospheric magnetic field, including both the local magnetic vector and the global configuration. To estimate how the PSD distributions are affected by different magnetic field models, we repeat the PSD computation over the above periods, by applying the best-fitting magnetic model, and the results are presented in Figure 6.

[29] Comparing the panels in Figure 6 to those in Figures 3, 4, and 5, we see that the main difference is in the L^* values. The discontinuity of L^* is obvious for both GEO and Polar in the case of best-fitting model, even during quiet time (the panels in column I of Figure 6), due to the lack of normalization between magnetic models. The same reason leads to the difference in the absolute values of L^* , e.g., the L^* 's for Polar at crossing 7 during quiet time are smaller in Figure 6 than those in Figure 3. During storms, more data points for Polar can sometimes be found in the plots for the best-fitting model, e.g., at crossing 9 of SP2001, which may be due to the fact that the magnetic field by T01s can be more stretched on the night side than other models and thus does not return a closed drift shell. Other than those differences, however, the overall features in the distributions are quite consistent: The relative positions of GEO and Polar, the time signatures of the loss and recovery in PSD, and the PSD radial gradients in the recovery phases. Such consistency provides us a rough sense of the reliability of the achieved PSD gradient results, and thus lays down the cornerstone on which a meaningful discussion of the energetic electrons source being external or internal is based.

4.2. Interpretation of Results

[30] For the two storm periods in Figures 4 and 5, though the loss of PSD in the main phase appears independent of energy, the recovery is quite an energy-dependent phenomenon: The recovery of electrons with low energy starts earlier and proceeds at a faster pace than that of electrons with high energy. It is explainable in both the external and internal scenarios. In a scenario with an external source that feeds electrons into radiation belts by inward diffusion, either the diffusion coefficient is energy dependent (the lower the energy, the larger the coefficient), or low-energy electrons start to diffuse inward earlier, or both. Actually, an energy dependent diffusion coefficient has been used by a diffusion model that successfully reproduces electron fluxes at GEO orbit [Li, 2004]. Nevertheless, even those models cannot explain the negative PSD radial gradient for the high-energy electrons observed at GEO. Another difficulty for diffusion models is that they require larger PSD at larger L^* shell in the recovery phases, which is not what is seen in the data, at least during these two storm periods. Conversely, an internal source can provide a straightforward explanation: Electrons are accelerated from low energy to high so that one always sees low-energy electrons first, and the source inside of GEO makes the negative radial gradient.

[31] By checking the PSD values during the storms in Figures 4, 5, and 6, we see that on average the GEO satellites always have larger PSD values than those of Polar during each recovery phase. Negative PSD gradients for electrons with the highest μ also prevail during almost all recovery phases. All those together strongly suggest that in situ acceleration plays a crucial role for the recovery of energetic electrons.

[32] However, PSD radial gradients in storms are frequently neither monotonically positive nor monotonically negative, instead they can have more than one maximum point, which possibly suggests a combined story. For example, electrons with low μ often have positive gradients at GEO during the recovery phases, indicating a source outside GEO orbit. In some cases when Polar by itself has a positive gradient, such as those in crossings 6 and 7 during SP2001 in Figure 4, it can be caused by intermittent injections from an external source separated by intervals of loss. In other cases that Polar has a smaller PSD, such as the crossing 7 during SP2002 in Figure 5, such radial profile can be caused by either an external source followed by a loss at Polar, or a source between GEO and Polar. (The energetic electrons trapped in the outer cusp [Sheldon *et al.*, 1998] have been proposed [Fritz *et al.*, 2000] to be able to diffuse through the magnetopause into the radiation belts and thus to serve as a source between GEO and Polar. However, when checking the GEO electron pitch angle distributions from the start of electron enhancement on 8 September 2002 until the crossing 7 during SP2002, we find no global signature of the butterfly distributions, which is associated with a minimum flux at the pitch angle of 90° and is expected to be seen when the electrons diffuse from the high latitude cusp region. Therefore the possibility of a source from the cusp can basically be ruled out, at least for the storms in this paper.)

[33] Compared to previous work, The positive gradients observed by Polar at crossings 6 and 7 in SP2001 are similar to those obtained by Green and Kivelson [2004] for storms when Polar passed on the nightside. In that paper, Green and Kivelson argued that it was caused by the poor performance of the magnetic field model on the nightside so that those positive gradients were not reliable. Here in this work, after adding PSD points from GEO to the distribution plot, we see that aside from the error caused by the magnetic field model, another factor is that the contributions from an internal source may not be seen by Polar at all at that time. In other words, a positive gradient at Polar does not have to exclude the possibility of an internal source.

4.3. Discussions on Polar and LANL GEO Data

[34] We have to admit that the ~ 14 -hour lapse between Polar crossings leave us some room for speculation before drawing any final and general conclusion from two case studies. For example, the involvement of loss processes can sometimes make it difficult to differentiate the source locations by simply identifying the PSD radial gradients. As being pointed out by Green and Kivelson [2004], an inward diffusion followed by a loss at large L^* can also produce a local maximum in the PSD radial profile which appears to be caused by an internal source. Since we cannot tell when a loss occurs at the large L shells during the lapses in Polar data, a conclusion of an internal source based on the negative PSD radial gradient at one Polar crossing can still be unreliable.

However, an indisputable evidence of an internal source is that the PSD value at GEO keeps on increasing with a negative radial gradient, such as the one after Polar crossing 3 in SP2001 as depicted in Figure 4c. Unfortunately, there is only one such example in this study. To draw a confirmative conclusion, we need to either extend this study of PSD distributions to data with a longer term or apply the results of this work to model simulations.

[35] The changing L^* values of GEO and Polar during storms also remind us that, for diffusion models using in situ measurements as boundary conditions, e.g., data from GEO satellites, it is necessary either to employ a nonfixed boundary with the raw data, with positions changing with the storm phases, or to convert the raw data to values at a fixed boundary. Otherwise, artificial loss and source will be introduced through the boundary and propagate over the calculation domain.

5. Conclusions

[36] Employing the method developed in our previous work, we have determined the storm time energetic electron phase space density radial distribution around the rim of the outer radiation belt by combining electron data from three LANL geosynchronous SOPA instruments with Polar CEP-PAD measurements. After the inter calibrations are accomplished during a quiet time, the calculation of electron PSD is undertaken for periods including the two GEM IM/S selected storms.

[37] Results for the two storm periods show that the enhancement of electron phase space density during storm recovery phases is energy dependent: Electrons with low energy start to recover earlier and have a faster recovery pace than electrons with high energy. Additionally, the energy dependent PSD radial gradients at GEO are also observed. They strongly indicate sources at different locations: Low-energy electrons are more likely to be replenished by a source outside of GEO, while the source for high-energy electrons is mainly from in situ acceleration, although sometimes an external source can contribute to the recovery, too.

[38] To draw a general conclusion from data, we plan to extend this study to a longer time period in the future and include measurements from more satellites. For modelers, results achieved in this paper can be used either as input or being compared with model calculations.

Appendix A: Derivation of PSD and Three Phase Space Coordinates (PSCs)

[39] After an appropriate magnetic field model is selected, the following equation [Hilmer *et al.*, 2000] is used in this work to convert the flux of each energy channel into the phase space density

$$f_{ch} = \left\{ \frac{j_{ch}}{\langle p^2 c^2 \rangle_{ch}} [1.66 \times 10^{-10}] \right\} \times 200.3 \quad (A1)$$

where j_{ch} is the flux in unit $s^{-1} cm^{-2} sr^{-1} keV^{-1}$, the terms in braces are equation (4) of Hilmer *et al.* [2000], and the multiplying factor is required to transform the PSD from

Table B1. List of Empirical External Magnetic Field Models

Model Name	Input Parameters	Valid Range
T89c: [Tsyganenko, 1989]	ψ, Kp	$r_{GEO} < 70R_e$
OP77: [Olson and Pfitzer, 1977]	ψ	$r_{GEO} < 15R_e$
OP88: [Pfitzer et al., 1988]	$dens, velo, Dst$	$r_{GEO} < 60R_e$
T96: [Tsyganenko and Stern, 1996]	ψ, Dst, P, By, Bz	$r_{GEO} < 40R_e$
OM97: [Ostapenko and Maltsev, 1997]	ψ, Dst, P, Bz, Kp	no limit
T01: [Tsyganenko, 2002a, 2002b]	ψ, Dst, P, By, Bz	$x_{GSM} > -15R_e$
T01s: [Tsyganenko et al., 2003]	ψ, Dst, P, By, Bz, Gs	$x_{GSM} > -15R_e$

Hilmer et al.'s unit to the GEM unit (c/MeV/cm)³ where c is the speed of light in a vacuum, and the term in the denominator is defined for each energy channel as

$$\langle p^2 c^2 \rangle_{ch} = \frac{1}{2} [K_{min}^{ch} (K_{min}^{ch} + 2m_0 c^2) + K_{max}^{ch} (K_{max}^{ch} + 2m_0 c^2)] \quad (A2)$$

where the K_{min}^{ch} and K_{max}^{ch} are the lower and upper limits of each energy channel in MeV, respectively, and $m_0 c^2$ is the rest energy of an electron. We define the energy of each channel as

$$E_{ch} = \sqrt{K_{min}^{ch} \cdot K_{max}^{ch}} \quad (A3)$$

considering a falling electron energy spectrum.

[40] In this paper, PSD is expressed in terms of three phase space momentum coordinates (μ, K, L^*) , which are associated with the three adiabatic invariants of the particle's motion. μ is the first invariant that corresponds to the cyclotron movement of electron around a field line and is given by

$$\mu = \frac{p_{\perp}^2}{2m_0 B} \quad (A4)$$

where p_{\perp} is the relativistic momentum component perpendicular to the local magnetic vector, m_0 is the rest mass of electron, and B is the local magnetic field magnitude. The second invariant has the original form of J that is associated with the bounce movement of electron along a field line:

$$J = 2\sqrt{2m_0\mu} \int_{S_m}^{S'_m} \sqrt{B_m - B(s)} ds \quad (A5)$$

where the subscript “ m ” indicates the mirror point, and B_m and $B(s)$ are the field strengths at the mirror point and point s , respectively, and ds is the distance along the field line. Since in J the term outside of the integration sign is a constant, another form of the second adiabatic invariant is

$$K = \int_{S_m}^{S'_m} \sqrt{B_m - B(s)} ds \quad (A6)$$

which is a magnetic field related quantity with no reference to particles and is appropriate when radially following a particle population that breaks the third adiabatic invariant but preserves K and μ . We use K in this paper.

[41] The L^* , Roederer L parameter, is defined as the radial distance to the equatorial location where an electron crosses if all external magnetic fields were slowly turned off leaving only an internal dipole field [Roederer, 1970]. It is associated with the third adiabatic invariant in the form of

$$L^* = \frac{2\pi M}{|\Phi| R_E} \quad (A7)$$

where M is the Earth's dipole magnetic moment, R_E is the Earth's radius, and Φ is the third invariant that is the magnetic flux through the electron's drifting shell.

[42] Besides the three momentum coordinates, a complete description of a particle's kinematical state requires three more positional coordinates, or so-called “phases”, (ϕ_1, ϕ_2, ϕ_3) which correspond to the three adiabatic motions. Each combination of $(\mu, K, L^*; \phi_1, \phi_2, \phi_3)$ describes a point in the six dimensional phase space. For a conserved system, Liouville's theorem demands a conserved distribution function along the path in phase space, which implies preserved PSD at constant (μ, K, L^*) with different (ϕ_1, ϕ_2, ϕ_3) so long as the adiabatic conditions are satisfied. For convenience, in this paper when we use the term “phase space coordinates,” we refer to the momentum coordinates only, that is, the combination of (μ, K, L^*) .

Appendix B: Best-Fitting Magnetic Field Model

[43] In a recently finished study of the PSD distribution around GEO orbit, we have tried a new scheme of using external magnetic field models. In this new scheme, instead of following the conventional way of sticking to one selected existing empirical model through the whole storm period, we first test all the existing field models in Table B1 by fitting to multipoint measurements of magnetic vectors during one given short time bin (e.g., 5 min here), and then one model with “the best performance” is selected for the PSD calculation from a given criterion. The dynamic magnetic model achieved in a such way is actually composed by several existing models and “jumps” from one to another for different times. Here we name it the best-fitting model.

[44] The fitting criterion is defined by

$$e_{BFM}^j = \min \left[\sum_i \left(w_i \frac{|\vec{B}_i - \vec{B}_{i,k=1}|}{|\vec{B}_i|} \right), \sum_i \left(w_i \frac{|\vec{B}_i - \vec{B}_{i,k=2}|}{|\vec{B}_i|} \right), \dots, \sum_i \left(w_i \frac{|\vec{B}_i - \vec{B}_{i,k=n}|}{|\vec{B}_i|} \right) \right] \quad (B1)$$

which means that in the time bin j , for the k_{th} magnetic field model, the error percentage between the model output $\vec{B}_{i,k}$ and in-situ measurement \vec{B}_i by satellite i is calculated and then is summed over all satellites, including GOES-8, GOES-10, Polar, and CLUSTER in that study; then from all models with $k = 1$ to n the one with the minimum error percentage e_{BFM}^j is selected to be the best-fitting model during the interval j . Here w_i is the weight function for satellite i and we use the same definition for all satellites which is

$$w(\vec{B}) = \begin{cases} 1 & : |\vec{B}| \geq 60nT \\ (|\vec{B}|/60)^3 & : \text{otherwise} \end{cases} \quad (B2)$$

where 60 nT is the threshold value of local magnetic field magnitude imposed to prevent the possible large error in weak field region, such as the tail through which CLUSTER crosses, being overweighted in the criterion function.

[45] A byproduct of the best-fitting model is the obtaining of the magnetic field model with the best performance statistically of fitting to multipoint magnetic field measurements. When counts of time bins for each magnetic model are binned to the Dst, the result shows that for quiescent times, with Dst within $[-30, 50]$ nT, several models including T01s compete to each other and have similar performance, all with reasonably low error percentages; while for storm times with Dst within $[-180, -30]$ nT, T01s has an outstanding performance and the largest chance (typically 60–80%) of providing the best fits to the measurements. Though this study can not be called a through one, since the selection criteria in equations (B1) and (B2) can be defined in different ways, the results strongly suggest that, among all models in Table B1, the T01s should be the best candidate model for storm times.

[46] **Acknowledgments.** This work was supported by the National Science Foundation's Geospace Environment Modeling Program. We thank T. Cayton and R. Christen for providing LANL GEO SOPA data. We are also grateful for the use of ONERA-DESP codes provided by D. Boscher and S. Bourdarie.

[47] Amitava Bhattacharjee thanks Michael Liemohn and another reviewer for their assistance in evaluating this paper.

References

- Belian, R., G. Gisler, T. Cayton, and R. Christensen (1992), High- z energetic particles at geosynchronous orbit during the great solar proton event series of October 1989, *J. Geophys. Res.*, **97**, 16,897–16,906.
- Blake, J. B., et al. (1995), CEPPAD: Comprehensive energetic particle and pitch angle distribution experiment on Polar, *Space Sci. Rev.*, **71**, 531–562.
- Chen, Y., R. Friedel, G. Reeves, T. Onsager, and M. Thomsen (2005), Multi-satellite determination of the relativistic electron phase space density at the geosynchronous orbit: Methodology and initial results in magnetic quiet times, *J. Geophys. Res.*, **110**, A10210, doi:10.1029/2004JA010895.
- Friedel, R., G. Reeves, and T. Obara (2002), Relativistic electron dynamics in the inner magnetosphere—A review, *J. Atmos. Solar Terr. Phys.*, **64**, 265.
- Friedel, R., S. Bourdarie, and T. Cayton (2005), Intercalibration of magnetospheric energetic electron data, *Space Weather*, **3**, S09B04, doi:10.1029/2005SW000153.
- Fritz, T., J. Chen, and R. Sheldon (2000), The role of the cusp as a source for magnetospheric particles: A new paradigm?, *Adv. Space Res.*, **25**, 1445–1457.
- Green, J., and M. Kivelson (2004), Relativistic electrons in the outer radiation belt: Differentiating between acceleration mechanisms, *J. Geophys. Res.*, **109**, A03213, doi:10.1029/2003JA010153.
- Hilmer, R., G. Ginet, and T. Cayton (2000), Enhancement of equatorial energetic electron fluxes near $L = 4.2$ as a result of high speed solar wind streams, *J. Geophys. Res.*, **105**, 23,311–23,322.
- Kanekal, S., D. Baker, J. Blake, B. Klecker, G. Mason, and R. Mewaldt (2000), Magnetospheric relativistic electron response to magnetic cloud events of 1997, *Adv. Space Res.*, **25**, 1387–1392.
- Kim, H., and A. Chan (1997), Fully-adiabatic changes in storm-time relativistic electron fluxes, *J. Geophys. Res.*, **102**, 22,107–22,116.
- Li, X. (2004), Variation of 0.7–6.0 MeV electrons at geosynchronous orbit as a function of solar wind, *Space Weather*, **2**, S03006, doi:10.1029/2003SW000017.
- Li, X., and M. Temerin (2001), The electron radiation belt, *Space Sci. Rev.*, **95**, 569–580.
- Olson, W., and K. Pfizter (1977), Magnetospheric magnetic field modeling, tech. rep., McDonnell Douglas Astronaut. Co., Huntington Beach, Calif.
- Ostapenko, A., and Y. Maltsev (1997), Relation of the magnetic field in the magnetosphere to the geomagnetic and solar wind activity, *J. Geophys. Res.*, **102**, 17,467–17,473.
- Pfizer, K., W. Olson, and T. Mogstad (1988), A time dependent source driven magnetospheric magnetic field model, *Eos Trans. AGU*, **69**, 426.
- Reeves, G., R. Belian, T. Cayton, M. Henderson, R. Christensen, P. McLachlan, and J. Ingraham (1997), Using Los Alamos geosynchronous energetic particle data in support of other missions, in *Satellite-Ground Based Coordination Source Book*, edited by M. Lockwood and H. Opgenoorth, pp. 263–272, ESA Publ., Noordwijk, Netherlands.
- Roederer, J. (1970), *Dynamics of Geomagnetically Trapped Radiation*, Springer, New York.
- Russell, C. T., R. C. Snare, J. D. Means, D. Pierce, D. Dearbourne, M. Larson, G. Barr, and G. Le (1995), The GGS/Polar magnetic field investigation, *Space Sci. Rev.*, **71**, 563–582.
- Schulz, M., and L. Lanzerotti (1974), *Particle Diffusion in the Radiation Belts*, Springer, New York.
- Sheldon, R., H. Spence, J. Sullivan, T. Fritz, and J. Chen (1998), The discovery of trapped energetic electrons in the outer cusp, *Geophys. Res. Lett.*, **25**, 1825–1828.
- Thomsen, M., D. McComas, G. Reeves, and L. Weiss (1996), An observational test of the Tsyganenko (T89a) model of the magnetospheric field, *J. Geophys. Res.*, **101**, 24,827–24,836.
- Tsyganenko, M. (1989), A magnetospheric magnetic field model with a wrapped tail current sheet, *Planet. Space Sci.*, **37**, 5–20.
- Tsyganenko, M. (2002a), A model of the near magnetosphere with a dawn-dusk asymmetry: 1. Mathematical structure, *J. Geophys. Res.*, **107**(A8), 1179, doi:10.1029/2001JA000219.
- Tsyganenko, M. (2002b), A model of the near magnetosphere with a dawn-dusk asymmetry: 2. Parameterization and fitting to observation, *J. Geophys. Res.*, **107**(A8), 1176, doi:10.1029/2001JA000220.
- Tsyganenko, M., and D. Stern (1996), Modeling the global magnetic field the large-scale Birkeland current system, *J. Geophys. Res.*, **101**, 187–27,198.
- Tsyganenko, M., H. Singer, and J. Kasper (2003), Storm-time distortion of the inner magnetosphere: how severe can it get?, *J. Geophys. Res.*, **108**(A5), 1209, doi:10.1029/2002JA009808.

Y. Chen, R. H. W. Friedel, and G. D. Reeves, Los Alamos National Laboratory, P.O. Box 1663, MS D466, Los Alamos, NM 87545, USA. (cheny@lanl.gov; rfriedel@lanl.gov; reeves@lanl.gov)